



Reactive HiPIMS deposition of Al-oxide thin films using W-alloyed Al targets

S. Kagerer^{a,*}, L. Zauner^{a,b}, T. Wojcik^a, S. Kolozsvári^c, T. Kozák^d, J. Čapek^d, P. Zeman^d, H. Riedl^{a,b}, P.H. Mayrhofer^a

^a Institute of Materials Science and Technology, TU Wien, A-1060 Wien, Austria

^b Christian Doppler Laboratory for Surface Engineering of High-performance Components, TU Wien, Austria

^c Plansee Composite Materials GmbH, D-86983 Lechbruck am See, Germany

^d Department of Physics and NTIS – European Center of Excellence, University of West Bohemia, Plzeň, Czech Republic

ARTICLE INFO

Keywords:

R-HiPIMS deposition
Alumina
Target poisoning
Polymorph structures

ABSTRACT

The outstanding oxidation resistance, thermo-mechanical stability, and chemical inertness of alumina, but also the synthesis of phase pure polymorphs attract particular attention in academia and industry. Especially, the difficulties regarding the synthesis of α - or γ -structured Al_2O_3 by physical vapor deposition techniques are still strong limitations. Within this study, we investigated in detail the influence of 2 at.% tungsten in the Al-target on the process stability and phase formation during reactive DC magnetron sputtering as well as high power impulse magnetron sputtering (HiPIMS) of Al_2O_3 -based coatings. The small addition of W to the Al target allows to increase the oxygen partial pressure by more than 200% while maintaining a stable deposition process. Ion mass spectroscopy measurements yield a promising high fraction of $^{16}\text{O}^+$ and $^{32}\text{O}_2^+$, when operating the W-containing target in the metal-to-poisoned transition mode. A significant increase of $^{16}\text{O}^+$ is further provided by the target surface oxide in poisoned mode. Detailed time-of-flight ion mass spectroscopy investigations during one HiPIMS pulse show a clear temporal separation of the individual ions arriving at the substrate plane during the pulse on-time, allowing for controlled ion attraction by synchronizing the bias pulse to the discharge impulse. Equal amounts of $^{27}\text{Al}^+$ and $^{32}\text{O}_2^+$ can be attracted using a bias on-time between 400 μs and 900 μs in the “off-time” (after glow) leading to a dense and nano-crystalline coating. Detailed electron microscopy investigations show the presence of metallic phase fractions for higher duty cycles (7.5%). Decreasing the duty cycle to 3.75% leads to amorphous coatings when operating the Al-target at the highest oxygen partial pressure in metallic mode.

1. Introduction

The preparation of alumina and different polymorphs of Al_2O_3 by means of physical vapor deposition (PVD) is within the focus of academic and industrial studies since decades [1–4]. Especially, the thermodynamically stable α -phase (corundum type) is highly interesting based on its inert and refractory character, being also stable in oxygen containing atmospheres up to 1700 °C. In the field of thin films and hard coatings also metastable structure types such as γ - or θ - Al_2O_3 [5,6] are of interest. For the latter structures, the energy barrier for their formation is lower than for α - Al_2O_3 , thus, typically during low-temperature depositions with their kinetic limitations during film growth, these metastable cubic structures are promoted [7].

To overcome the most prevalent challenges during PVD-based

synthesis of Al_2O_3 related coatings – i.e., high deposition temperatures as well as limited electrical conductivity (resulting from massive target poisoning during reactive synthesis) – various deposition approaches have been established in general: (i) usage of ceramic Al_2O_3 -based target materials in non-reactive atmospheres [8], (ii) reactive sputtering of pure Al targets in oxygen containing gas mixtures [9–11], (iii) utilization of alloyed Al-targets to stabilize specific phases in reactive depositions (e.g., Cr or Fe to promote the α -phase [12]), as well as (iv) an increase in ionization rate of Al and O species to promote a stoichiometric phase formation [13]. However, each approach exhibits specific advantages and drawbacks. Non-reactive depositions typically suffer from low deposition rates, as the isolating target needs a periodic operation, typically applied in the form of radio-frequency sputtering [8]. The formation of an isolating layer with low sputtering yield on Al targets during reactive

* Corresponding author.

E-mail address: stefan.kagerer@tuwien.ac.at (S. Kagerer).

<https://doi.org/10.1016/j.surfcoat.2021.127467>

Received 15 February 2021; Received in revised form 10 June 2021; Accepted 25 June 2021

Available online 30 June 2021

0257-8972/© 2021 The Author(s). Published by Elsevier B.V. This is an open access article under the CC BY license (<http://creativecommons.org/licenses/by/4.0/>).

sputtering leads to arcing events and pronounced hysteresis effects, being the main drawbacks of reactive processes [14,15]. A hysteresis-free deposition of α - Al_2O_3 was proposed by Wallin et al. [13,16] when using high power impulse magnetron sputtering (HiPIMS). This technique allows for high ionization fractions of Al as well as O_2 species, fostering the growth of uniform and dense coatings. However, a completely hysteresis-free deposition can only be achieved with a sufficient pumping speed of the deposition system [17], which is typically not the case for larger, industrial-sized applications. Then, the utilization of a gas-feedback control system is necessary, which provides stable discharge conditions with respect to target poisoning [18]. Moreover, through the utilization of HiPIMS the deposition rate decreases drastically [19]. Another promising approach to deposit corundum-type alumina is to use alloyed Al-targets. The most famous and well-studied approach in this regard is the use of $\text{Al}_{0.70}\text{Cr}_{0.30}$ targets, which also allow for cathodic arc evaporation (CAE) [20]. In addition to the strong α -phase stabilizer Cr, also Si or B alloying specifically retards target poisoning or promotes the crystallization of Al_2O_3 polymorphs [15].

With a specific experimental set-up, Berg et al. [21] proved that Pt implantations increase the erosion rate of Si and C drastically. The so-called atom assisted sputter yield amplification influences the depth of the collision cascade so that surface near species are more effectively sputtered from the target. Further studies showed that tungsten co-sputtering on an aluminum target increases the deposition rate by up to 80% and allows deposition processes with higher oxygen flows as compared to unalloyed Al targets [22]. This sputter yield amplification just lead to an incorporation of 1 at.% tungsten within the film. In addition, density functional theory (DFT) studies suggest that small amounts of dopants can even further promote the formation of α - and θ -alumina. In particular, transition metals such as W and Mo stabilize the θ -phase, which implies that alumina can be formed also at lower deposition temperatures. The phase transformation towards α -structured morphologies can be retarded, as long as the dopants are not accumulating through diffusion [23]. Recently we showed that targets alloyed with 2 and 5 at.% transition metals increases the usage of high oxygen partial pressures. Especially W and Cr dopants (2 at.%) increase the mechanical properties, the deposition rate, as well as the process stability, allowing to run the targets at high oxygen partial pressures even during DC magnetron sputtering (DCMS) [24].

Based on these results, we studied the reactive HiPIMS process using both a W-alloyed and an unalloyed Al target in comparison with DCMS. This allowed to not only shift the target poisoning to higher oxygen gas flows, but simultaneously also to increase the ion flux to assist the growth of Al_2O_3 coatings.

2. Experimental

All $\text{Al}_{2\pm\delta}\text{O}_{3\pm\delta}$ and $(\text{Al}_{0.98}\text{W}_{0.02})_{2\pm\delta}\text{O}_{3\pm\delta}$ thin films were synthesized with an “in-house” developed reactive magnetron sputtering system (details are described in Ref. [25]). This system is equipped with two 6-in. cathodes (Gencoa Ltd.) operated with Solvix HiP³ 5 kW DC/HiPIMS generators, and two 3-in. cathodes (Gencoa Ltd.) operated with MKS ENI RPG-50 5 kW generators. In this study we used the two 6-in. cathodes equipped with powder metallurgically prepared targets (Plansee Composite Materials GmbH, purity of 99.8 at.%), one Al and one $\text{Al}_{0.98}\text{W}_{0.02}$ target. The substrates, double-side polished (100)-orientated silicon platelets ($20 \times 7 \times 0.38 \text{ mm}^3$), were cleaned for 10 min in an ultrasonic bath of acetone and ethanol consecutively, before mounting in the deposition chamber and heating to the deposition temperature of $T_{\text{sub}} = 280 \text{ }^\circ\text{C}$ (measured directly on the substrate plane). After 20 min at this temperature, the substrates were ion etched in Ar atmosphere at a pressure of 6 Pa for 10 min applying a substrate potential of -500 V DC (MKS ENI RPG-50 5 kW generator). During the deposition, the substrates were held at $280 \text{ }^\circ\text{C}$, with the substrate holder rotating at 90 rad/s (0.25 Hz). The distance between the confocally aligned cathodes and the substrate holder was about 108 mm. Various Al and $\text{Al}_{0.98}\text{W}_{0.02}$ based

oxide-coatings were deposited using the respectively operated cathodes at an Ar pressure of $p_{\text{Ar}} = 0.4 \text{ Pa}$ (Ar flow = 25 sccm), a bias potential of $U_{\text{bias}} = -50 \text{ V DC}$, while systematically changing the $\text{O}_2/(\text{O}_2 + \text{Ar})$ flow rate ratio. Discharge frequencies f of 250, 500, and 1000 Hz were applied while keeping the negative voltage pulse length (on-time, t_{on}) constant at $75 \text{ }\mu\text{s}$, resulting in duty cycles of 1.875%, 3.75%, and 7.5%. The average target power was adjusted so that all HiPIMS depositions were carried out near to or within the HiPIMS regime but at least with an averaged target power of 16 W/cm^2 , which results in different peak power densities corresponding to the applied frequency and the poisoning state of the target (see Fig. 1).

The chemical compositions of the $(\text{Al}_{0.98}\text{W}_{0.02})_{2\pm\delta}\text{O}_{3\pm\delta}$ coatings were obtained by energy-dispersive X-ray spectroscopy (EDS, FEI Philips XL30 with an EDAX EDS detector at 20 kV accelerating voltage). For scanning electron microscopy (SEM) investigations we used a FEI Quanta 200 SEM equipped with a field emission gun to advise the morphology of the fracture cross sections of coated silicon substrates. Transmission electron microscopy (TEM) of cross-sectionally prepared samples (through mechanical- and subsequent ion-polishing) was performed on a TECNAI F20 FEG TEM equipped with an EDAX Apollo XLT 2 detector, which was also operated in high resolution (HR-TEM) as well as in scanning mode (STEM) for detailed structural and chemical analysis. In addition, selected area electron diffraction (SAED) patterns were acquired, using apertures with either 650 or 170 nm diameter to select the regions of interest.

Detailed plasma diagnostics during the HiPIMS process of the Al and $\text{Al}_{0.98}\text{W}_{0.02}$ targets were conducted with mass-, time-, and energy-resolved spectroscopy measurements. These measurements were carried out in a separate cylindrical vacuum chamber (506 mm in diameter and 522 mm in height), pumped by a diffusion pump, and equipped with a 4-in. magnetron (VTech, Gencoa Ltd). The magnetic field strength was adjusted to reproduce the discharge characteristics of the actual deposition system utilized for the Al_2O_3 -based films. The base pressure was below $2 \times 10^{-3} \text{ Pa}$, and the Ar pressure was set to 0.4 Pa (17 sccm) using a throttle valve between chamber and diffusion pump. After the discharge ignition, oxygen was added to with a flow rate between 0 and 10 sccm (leading to a small rise in total pressure up to 0.6 Pa). The magnetron was driven with a high-power pulsed direct current power supply (SIPP2000USB, Melec GmbH), able to operate also in DC mode. The average discharge power was set constant to 840 W either in DC or HiPIMS mode (being equivalent to 1 kW/cm^2). In the latter case, the negative voltage pulse length was set to $75 \text{ }\mu\text{s}$ and the pulse repetition frequency was 250, 500, or 1000 Hz. The waveforms of the target voltage and current were recorded using a digital oscilloscope (PicoScope 5444D, Pico Technology). The discharge plasma was analyzed by an energy-resolved mass spectrometer (Hiden Analytical EQP300) whose sampling orifice was directly facing the center of the target at a target-orifice distance of 150 mm. The mass spectrometer was tuned to $^{40}\text{Ar}^+$ ions and the obtained setting was kept constant for all measurements. Standard time-averaged acquisitions of ion energy spectra were measured for $^{40}\text{Ar}^+$, $^{40}\text{Ar}^{2+}$, $^{27}\text{Al}^+$, $^{32}\text{O}_2^+$ and $^{16}\text{O}^+$ ions. The extractor voltage was set to -40 V with respect to ground potential and the electrode controlling the ion energy was scanned from -40 to $+40 \text{ V}$, which ensured that all ions (with different energies) were recorded during the measurement. We observed that the dominant peak in the ion energy distribution function shifts to negative values with respect to the grounded mass spectrometer as the oxygen partial pressure in the chamber increases. We believe this indicates that the plasma potential around the mass spectrometer slightly decreases as the mass spectrometer body is covered by the insulating compound which inhibits the flow of electron current through the mass spectrometer. The dwell time for ion detection at each point was 10 ms. For each species, the scan over the energy range was repeated 5 times to increase the signal-to-noise ratio and to identify potential long-term changes in the discharge conditions during the measurement. Total ion count was calculated for each species and discharge regime by integrating the energy spectra over the whole

energy range. Moreover, time-resolved ion counts were measured for selected HiPIMS regimes. The mass spectrometer was set to continuously scan one species at a narrow energy range (typically 20 eV) corresponding to the peak in the ion energy distribution function with a dwell time of 100 ms. The raw pulse-stream output of the ion detector was brought to a multichannel scaler (SR430, Stanford Research Systems). This device registered the incoming pulses and accumulated them successively in evenly spaced time intervals once a trigger signal for the negative voltage pulse of the HiPIMS power supply was registered. Thus, the time of arrival of ions onto the detector with respect to the beginning of the negative pulse was discriminated with a time resolution of 1.28 μ s (width of the accumulation-time interval). A correction for the time-of-flight of ions in the mass spectrometer [26,27] was applied during post-processing of the data. Several tens of thousands of pulse periods were accumulated to increase the signal-to-noise ratio.

3. Results and discussions

According to A. Anders [28], the peak power density (p_{peak}) is supposed to be at least 2 orders of magnitude higher than the time-averaged power of HiPIMS discharges to ensure a high probability for ionization within the plasma. Therefore, we plotted the peak power density of each discharge condition in relation to the duty cycle, see Fig. 1. The indicated power limits are taken from [28–31]. The red line indicates our system limit with respect to power as well as cooling water temperature. Due to physical cooling restrictions, the upper limit for DCMS/pulsed-DCMS is typically located in the range of $p_{peak} = 0.05$ kW/cm². Based on this assumption, depositions with peak power densities above this value are classified in the transition region (i.e. values typically associated with modulated pulsed power (MPP) deposition). Furthermore, the HiPIMS regime is entered at $p_{peak} \sim 0.5$ kW/cm². In general, higher peak power densities are accompanied by lower duty cycles [30]. To vary the peak power density, the discharge frequency (250 Hz, 500 Hz, and 1000 Hz at constant $t_{on} = 75$ μ s, resulting in duty cycles of 1.875, 3.75, and 7.5%, respectively) and the oxygen partial pressure (p_{O_2} was varied between 0.005 and 0.24 Pa through gas flow variations from 4 to 24 sccm O₂ at constant Ar flow of 25 sccm) were varied systematically when sputtering

the Al_{0.98}W_{0.02}-target. For all nine discharge conditions the average power was set to 3.3 kW and the O₂ + Ar gas mixture was introduced to the chamber via gas inlets located 1 cm above the target surface. Consequently, all discharges with a duty cycle of 7.5% (1000 Hz) are located well-within the transition regime (see Fig. 1, blue data points). The O₂ partial pressures of the deposited coatings were 0.06 Pa, 0.15 Pa and 0.24 Pa, respectively (see Fig. 1, blue, half-filled squares). The coatings marked with T^P are coatings deposited in transition mode on the way to poisoned mode with respect to the target surface chemistry (i.e. at increasing O₂ flow rate ratio). These points describe the last stable working point using the highest p_{O_2} before the target potential abruptly decreases to attain the poisoned state. Contrary the coatings marked with P^T are defined as the points with the lowest p_{O_2} on the hysteresis curve, being the first stable working point before the target potential abruptly increases again to attain the metallic state (i.e. at decreasing O₂ flow rate ratio). Coatings marked with T were directly deposited in the transition mode. A schematic illustration of this notation with regard to a typical hysteresis curve is additionally presented in Fig. 3a. Due to the difference in the chamber geometry the partial pressures for the plasma diagnostics were slightly adapted, with the corresponding discharge data points displayed as blue, open squares in Fig. 1.

Decreasing the frequency to 500 Hz leads to higher peak power densities and a lower duty cycle (3.75%) – see orange, half-filled and open circles in Fig. 1. Here, for the depositions conducted with the higher oxygen containing atmospheres ($p_{O_2} = 0.095$ and 0.14 Pa) the HiPIMS regime is already entered, while for $p_{O_2} = 0.04$ Pa as well as all discharge conditions used for the plasma diagnostics, processes were still operating within the transition region. For the discharges operated at 250 Hz, all depositions (prepared with $p_{O_2} = 0.04$, 0.075, and 0.09 Pa – green, half-filled stars in Fig. 1) as well as the discharge conditions of the plasma diagnostics (see Fig. 1, green, open stars) are within the HiPIMS regime. Generally, with increasing p_{O_2} ($P^T < T < T^P$) the peak power density increases, which is in agreement with previous studies [32], and hence for $f = 500$ Hz and 250 Hz, the HiPIMS regime could be entered. This effect is directly linked to the poisoning state of the target surface [33,34], as thereby the current during one pulse increases resulting in overall higher peak power densities. Contrary to earlier reports, a hysteresis-free deposition of Al₂O₃ (as described in Refs. [13,16]) was not achieved during our HiPIMS studies. We envision that this strongly depends on the size of the deposition chamber, where smaller systems allow for a narrower hysteresis, but also the too low pumping speed of our deposition facility, which was lower than a critical pumping speed necessary to successfully suppress hysteresis [35,36].

The hysteresis behavior of the Al as well as the Al_{0.98}W_{0.02} target during DCMS and HiPIMS, see Fig. 2, was recorded with an average peak power density of 1 kW/cm² using the above-described chamber (equipped with a 4-in. magnetron). As mentioned, the argon flow was kept at 17 sccm ($p_{Ar} = 0.4$ Pa) while the oxygen flow rate was gradually increased until the target was fully in the poisoned mode. At each individual oxygen flow rate, measurements of the discharge were conducted after reaching a steady state behavior. Here, the target voltage is used to describe the hysteresis behavior. The blue lines in Fig. 2a-d represent the hysteresis curves of the pure Al-target, which is for all sputtering conditions (DCMS in Fig. 2a and HiPIMS with $f = 1000$, 500, and 250 Hz in Figs. 2b, c, and d, respectively) narrower than that of the Al_{0.98}W_{0.02}-target, represented by red lines. Furthermore, not only becomes the hysteresis curve wider when alloying W to the Al-target, also the onset of the poisoned state (P) is shifted to higher oxygen partial pressures, e.g., from $p_{O_2} \sim 0.096$ to 0.16 Pa (~ 6 to 10 sccm O₂) during DCMS. This effect is caused by the significantly increased sputter rates [21,22,24] due to the sputter yield amplification induced by evenly distributed heavy W atoms within the Al target, thereby consuming a larger fraction of the available reactive gas in the vapor phase. Also the back-attraction of these heavy W ions (having too low energies for leaving the attraction-range of the target potential) to the target surface – there causing sputtering of the continuously forming isolating surface

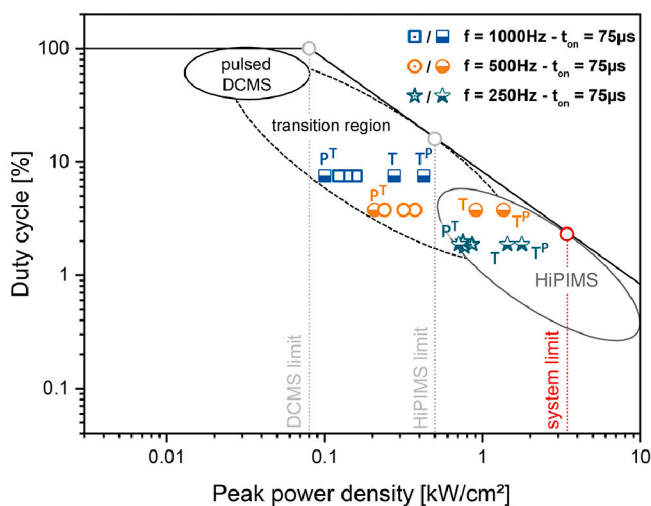


Fig. 1. Deposition conditions used in this study in relation to the DCMS, the transition, and the HiPIMS region, which are indicated based on the established terminology for pulsed discharge techniques and established power limits given in [26–28]. Within each of the three-deposition series with $f = 1000$, 500, and 250 Hz, the three half-filled symbols labelled with P^T, T, and T^P represent the deposition conditions used to prepare the coatings from targets operating in poisoned to transition mode, transition mode, and transition to poisoned mode, respectively. The open symbols represent the process conditions used for ion mass spectroscopy, whereas the half-filled ones denote the deposited coatings.

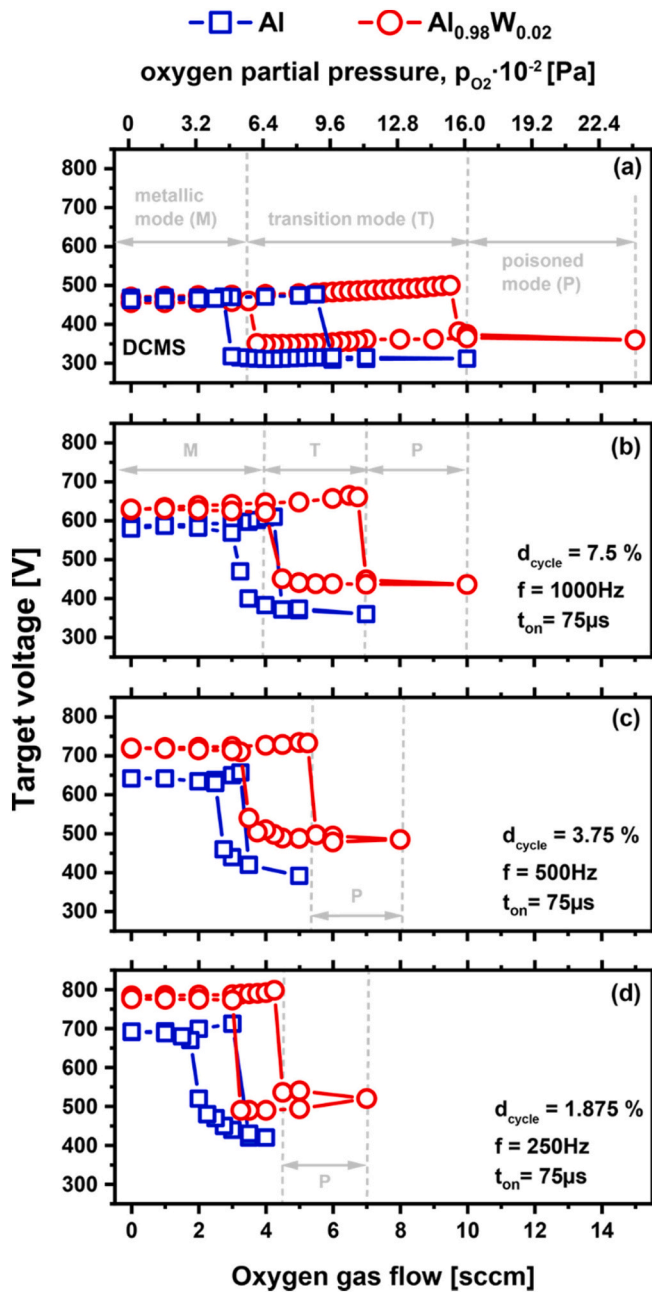


Fig. 2. Target voltage as function of the oxygen gas flow, presenting the hysteresis effect during poisoning of a pure Al-target (blue square symbols and lines) and an $Al_{0.98}W_{0.02}$ -target (red circle symbols and lines) for (a) DCMS and HiPIMS operated at a pulse frequency of (b) 1000 Hz, (c) 500 Hz, and (d) 250 Hz.

oxide – can be interpreted as an additional supportive effect for shifting the onset of target poisoning [17,36]. The corresponding behavior is also observed during HiPIMS operation (see Figs. 2b-d). In addition, with decreasing frequencies during HiPIMS, a shift in the target potential differences between the pure Al and the $Al_{0.98}W_{0.02}$ target as well as the overall potentials of both target types increase as a result of higher pulse power densities due to lower t_{on}/t_{off} ratios.

In general, all pulsed regimes lead to narrower transition zones (T) and earlier poisoning onsets in HiPIMS compared to DCMS in accordance with Ref. [17]. For both target materials, the onset of poisoning shifts to lower O_2 flow rates with decreasing duty cycle (*i.e.* decreasing frequencies for constant t_{on}). In terms of process stability and controllability of the transition or poisoned mode, the tungsten alloyed target

clearly outperforms the pure Al counterpart with respect to the overall oxygen partial pressure. This becomes especially clear when regarding the onset of the poisoned regime for the $Al_{0.98}W_{0.02}$ target which is located at O_2 flows where an operation of the Al target already involved arcing at the target – *e.g.*, Fig. 2c at 5 sccm O_2 ($p_{O_2} = 0.08$ Pa) for 3.75% duty cycle ($f = 500$ Hz).

In addition to the poisoning behavior, also the ion distribution during DCMS as well as HiPIMS of the Al and the $Al_{0.98}W_{0.02}$ target is different. Three representative deposition conditions (*i.e.*, T^P transition to poisoned mode, T transition mode, and P^T poisoned to transition, schematically shown in Fig. 3a) were selected and analyzed with respect to ion formation for DCMS (see Fig. 3a) and HiPIMS discharges having duty cycle of 7.5% ($f = 1000$ Hz, see Figs. 4a-b) and 3.75% ($f = 500$ Hz, see Fig. 4c), respectively. As mentioned above, the highest p_{O_2} on the hysteresis curve was chosen for T^P , marked by a blue circle in Fig. 3a. Accordingly, the lowest p_{O_2} of the hysteresis was chosen for P^T , before the target potential again steeply increased towards the metallic mode (marked by a red circle). For the transition condition T, the O_2 flow was set between these two extremes and the power supply was operated in a constant voltage mode. This allowed the discharge operation at the point indicated by a grey circle in Fig. 3a.

Between the Al and the $Al_{0.98}W_{0.02}$ target there is no significant difference in the total ion counts recorded during DCMS, except for the generally lower emission of $^{16}O^+$ (purple, half-filled circles) in the transition mode and P^T mode from the $Al_{0.98}W_{0.02}$ target (see Figs. 3b and c). This could be explained by the increased sputter rate of Al from the $Al_{0.98}W_{0.02}$ target, where the larger flux of Al atoms entering the plasma results in a quenching of the electron temperature due to the low first ionization energy of Al ($IE_{1,Al} = 5.98$ eV [37]), consequently decreasing the probability for an ionization of O atoms ($IE_{1,O} = 13.62$ eV [25,37]). Additionally, this explanation is underlined by a slight increase in the Al^+ -ion counts observed for the P^T mode. Also, the increased sputtering rate of Al from the $Al_{0.98}W_{0.02}$ target likely results in a more metallic target surface. Thus, less oxygen is sputtered from the target which contributes to the above-mentioned trend in the ion counts.

In general, all ion counts increase by an order of magnitude when operating both targets in a HiPIMS discharge (compare Figs. 3b and c with Figs. 4a and b), the waveforms for the respective HiPIMS discharges are given in the appendices (B). Analogous to the DCMS case, we observe a significant decrease in the $^{16}O^+ / ^{32}O_2^+$ ion count ratio (see the difference between the red curve, O_2^+ , and the violet curve, O^+ , getting larger) when the $Al_{0.98}W_{0.02}$ target is used instead of the pure Al target. When taking the Al^+ ion counts into account, the results are inconclusive as the ratio between $^{27}Al^+$ ion counts and $^{32}O_2^+$ metal ion counts is similar for all regimes on both targets, see Fig. 4a and b. However, considering that the ion counts for W remain fairly unaffected throughout all modes, with W also having a reasonably low first ionization energy ($IE_{1,W} = 7.86$ eV [37]), a possible interpretation for the lower ion counts of $^{16}O^+ / ^{32}O_2^+$ on the $Al_{0.98}W_{0.02}$ target may be given.

For a duty cycle of 3.75% ($f = 500$ Hz), the ion counts from the $Al_{0.98}W_{0.02}$ target are especially different between the T^P mode and transition mode, indicating the distinct differences in target and discharge state. The results further show that the probability for ionization events involving oxygen species is significantly lower in the T^P mode at a reduced duty cycle, which also hints an overall lower amount of O_2 available – compare open circles ($^{32}O_2^+$) and half-filled circles ($^{16}O^+$) between Fig. 4b and c. On the other hand, for both frequencies ($f = 500$ and 1000 Hz), the relative ratio between $^{32}O_2^+$ and $^{16}O^+$ remains very similar. In general, a high contribution from $^{32}O_2^+$ and $^{16}O^+$ ions in the total ion flux onto the substrate plane is recorded throughout all operating regimes, yet especially in the transition and the P^T mode. This is due to the increased oxygen partial pressure in these regimes, since less oxygen is consumed by metal species onto the chamber walls. The $^{16}O^+$ ions detected by the mass spectrometer could originate from O_2 molecules by dissociation and subsequent ionization in the high-density plasma in front of the magnetron or by ionization of single O atoms sputtered from the oxidized target. Due to

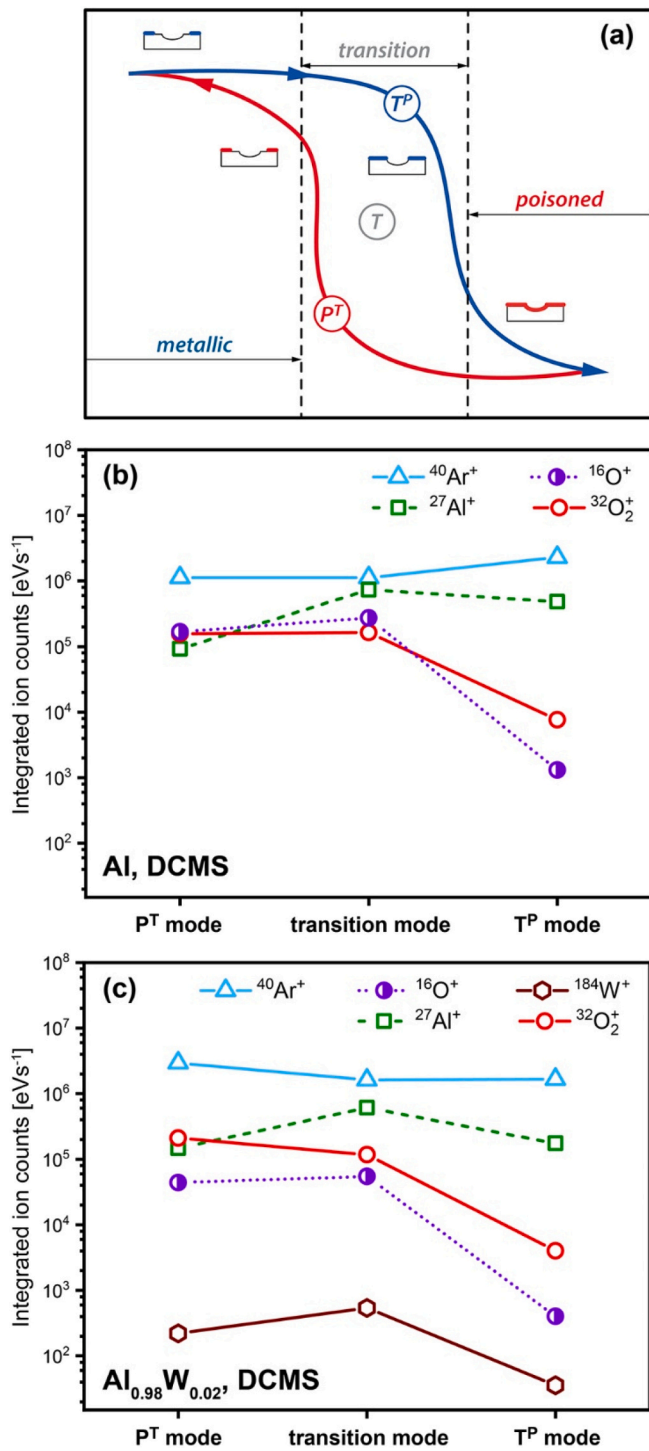


Fig. 3. (a) Schematic illustration of a typical hysteresis curve for Al operated in Ar/O₂ atmosphere including the relative positions of the target modes (“transition to poisoned mode” T^P, transition mode T and near “poisoned to transition” mode P^T) utilized to indicate the discharge conditions for the conducted plasma diagnostics and thin film depositions. Integrated ion counts recorded during DC magnetron sputtering of an (b) Al- and (c) Al_{0.98}W_{0.02}-target operated in T^P, transition, and P^T mode.

the fact that the secondary electron emission increases with increasing oxidation of the Al target, higher peak plasma densities were obtained for targets operated in the transition and P^T mode compared to the T^P mode, resulting in a higher ionization fraction and dissociation of the plasma species. The metal and Ar ions, $^{27}\text{Al}^+$, $^{184}\text{W}^+$, and $^{40}\text{Ar}^+$, show only a weak

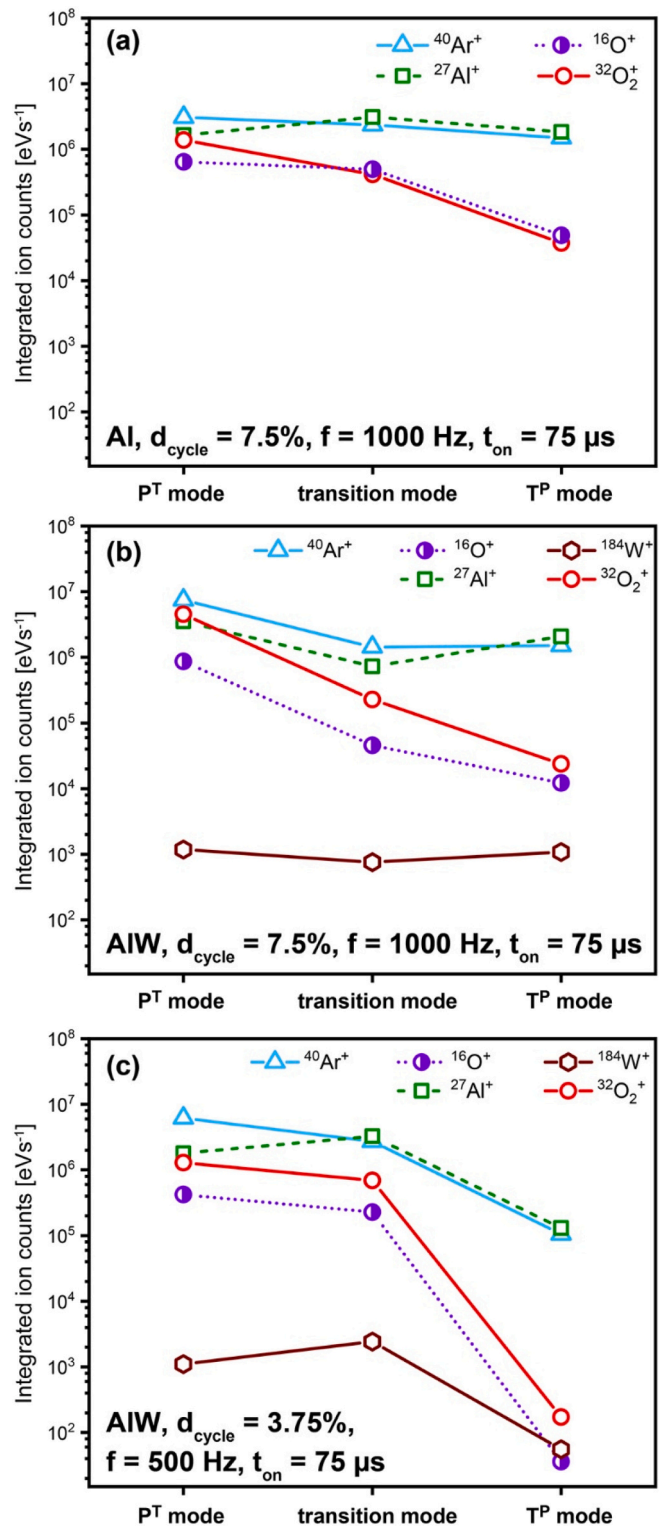


Fig. 4. Integrated ion counts recorded during operation of (a) an Al target and (b) an Al_{0.98}W_{0.02} target at $f = 1000\text{ Hz}$ in P^T, transition, and T^P mode. Furthermore, (c) integrated ion counts for an Al_{0.98}W_{0.02} target operated at $f = 500\text{ Hz}$ in P^T, transition, and T^P mode are shown.

dependency on the target-operating-mode as well as the duty cycle (here variable frequency at constant t_{on}). However, our data suggests that for the lower duty cycle (3.75% or $f = 500\text{ Hz}$) the number of these ions nearly increases by one order of magnitude when changing from T^P mode to transition or P^T mode, Fig. 4c.

More detailed studies of the discharge conditions were conducted via time-resolved time-of-flight (TOF) ion mass spectroscopy when operating the $\text{Al}_{0.98}\text{W}_{0.02}$ target between the transition and HiPIMS region (see Fig. 1, duty cycle of 7.5%, $f = 1000$ Hz) at $p_{\text{O}_2} = 0.1$ Pa. Fig. 5a shows an overview of the time-resolved ion distribution during one full discharge cycle, whereas Fig. 5b presents a detailed view of the discharge on-time (highlighted in grey in Figs. 5a-b) and the initial timeframe after the cathode shutdown. For oxygen ion species, basically only a single, cumulative peak exists inside the cathode on-time ($t = 40\text{--}75$ μs), whereas the ion counts for Al show a second, lower maximum in addition to the one at the pulse end ($t \sim 75$ μs), which is located slightly after the on-time ($t \sim 130$ μs). After the cathode pulse ignition, the distribution also presents an initial Ar-ion peak ($t = 10$ μs), which fluctuates over the entire pulse duration, to then steadily decrease during the off-time between pulses. Interestingly, the number of molecular O_2^+ ions shows – after an initial decrease with the cathode shutdown – an increasing trend during the off-time. Contrary, the number of atomic O^+ ions continuously decrease in the afterglow regime. This seems plausible considering that atomic O^+ ions can be generated from formed oxides at the target surface, but molecular O_2^+ ions can be formed from the gas further away from the target and also the constant presence of O_2^+ can be explained by the recombination of O^+ . Based on these data, a bias pulse [25,38] with an on-time synchronized between 400 and 900 μs after the target pulse may be utilized to especially attract $^{32}\text{O}_2^+$ ions and Al^+ ions supported by a high fraction of Ar^+ ions to facilitate the growth of an Al-oxide thin films. This time frame supposes that the relatively short and intense Ar^+ input compared to longer off-sets (see 500 Hz, $t_{\text{on}} = 75$ μs , $t_{\text{off}} = 1925$ μs) support the $^{32}\text{O}_2^+$ ions and Al^+ ions stream and lead to a densification of the microstructure. Accordingly, the chemistry of the coating is basically influenced by $^{32}\text{O}_2^+$ ions and Al^+ ions. On the other hand, during the pulse on-time of the cathode pulse (see Fig. 5b), the ions Ar^+ , O_2^+ , O^+ , and Al^+ can hardly be attracted individually by a synchronized bias potential due to a lack of distinct temporal separation between the ion flux maxima. Here again, the very similar TOF behavior of O^+ and Al^+ (both distributions revealing a simultaneous peak at the end of the on-time, $t \sim 75$ μs) suggests that both species originate at or near the target surface and are transported in a similar way towards the detection orifice, i.e. the substrate surface. Molecular O_2^+ ions obtain a peak influx almost in the center of the on-time ($t \sim 40$ μs). Hence, to support the attraction of O^+ ions, a synchronized bias pulse should have an on-time between 60 and

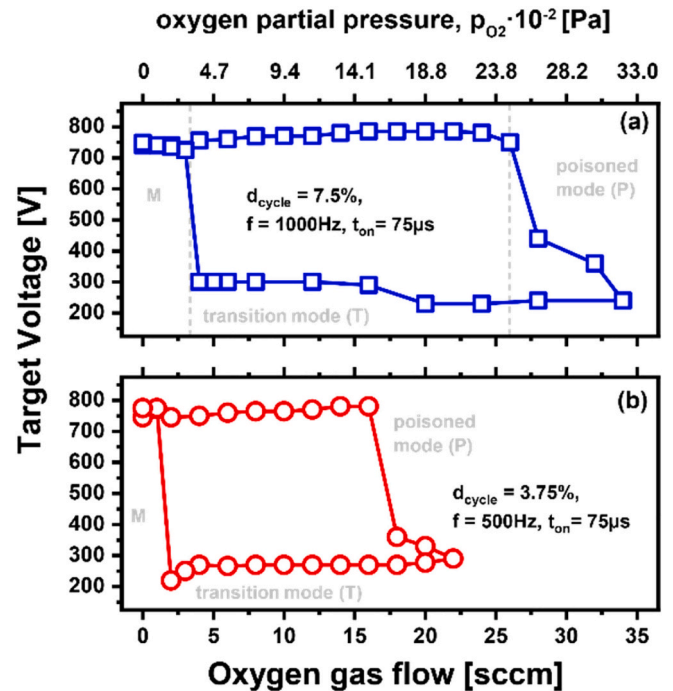


Fig. 6. Target voltage evolution as function of the oxygen gas flow for an $\text{Al}_{0.98}\text{W}_{0.02}$ -target operated by HiPIMS with (a) $f = 1000$ Hz and (b) $f = 500$ Hz within the deposition system used to prepare the coatings. Both graphs display the typical hysteresis behavior observed during poisoning of a target surface.

100 μs after the target-pulse. Contrary a bias pulse with an off-time between 60 and 100 μs , will specifically support O_2^+ ion attraction.

Based on these findings we prepared coatings using a large lab-based deposition chamber with $f = 500$ Hz ($t_{\text{on}} = 75$ μs , duty cycle = 3.75%) at oxygen partial pressures of 0.14, 0.095 and 0.04 Pa from the $\text{Al}_{0.98}\text{W}_{0.02}$ target. The oxygen partial pressures applied correspond to the three selected target poisoning states T^{P} mode, transition mode, and P^{T} mode, respectively (see definition in Fig. 3a), and are adjusted to the hysteresis curve recorded for this deposition chamber and discharge settings (see Fig. 6).

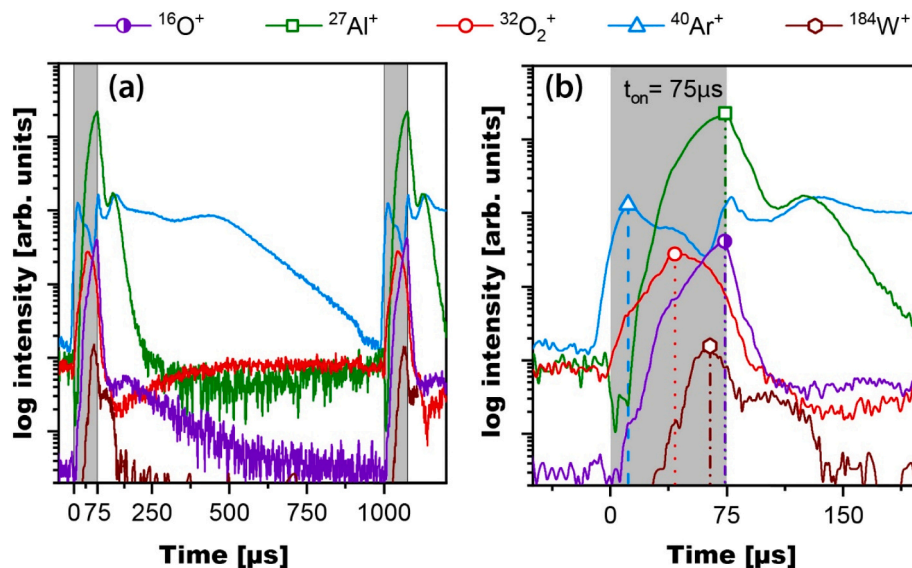


Fig. 5. (a) Time-of-flight ion mass spectroscopy measurements during operation of an $\text{Al}_{0.98}\text{W}_{0.02}$ target at $f = 1000$ Hz ($t_{\text{on}} = 75$ μs , duty cycle = 3.75%) and an O_2 partial pressure of 0.1 Pa. (b) Detailed view of the cathode operating time (indicated by a grey background) as well as the initial timeframe after the cathode shutdown. Additionally, the maxima of all individual ion fluxes recorded are indicated with respect to the pulse ignition at $t = 0$ μs .

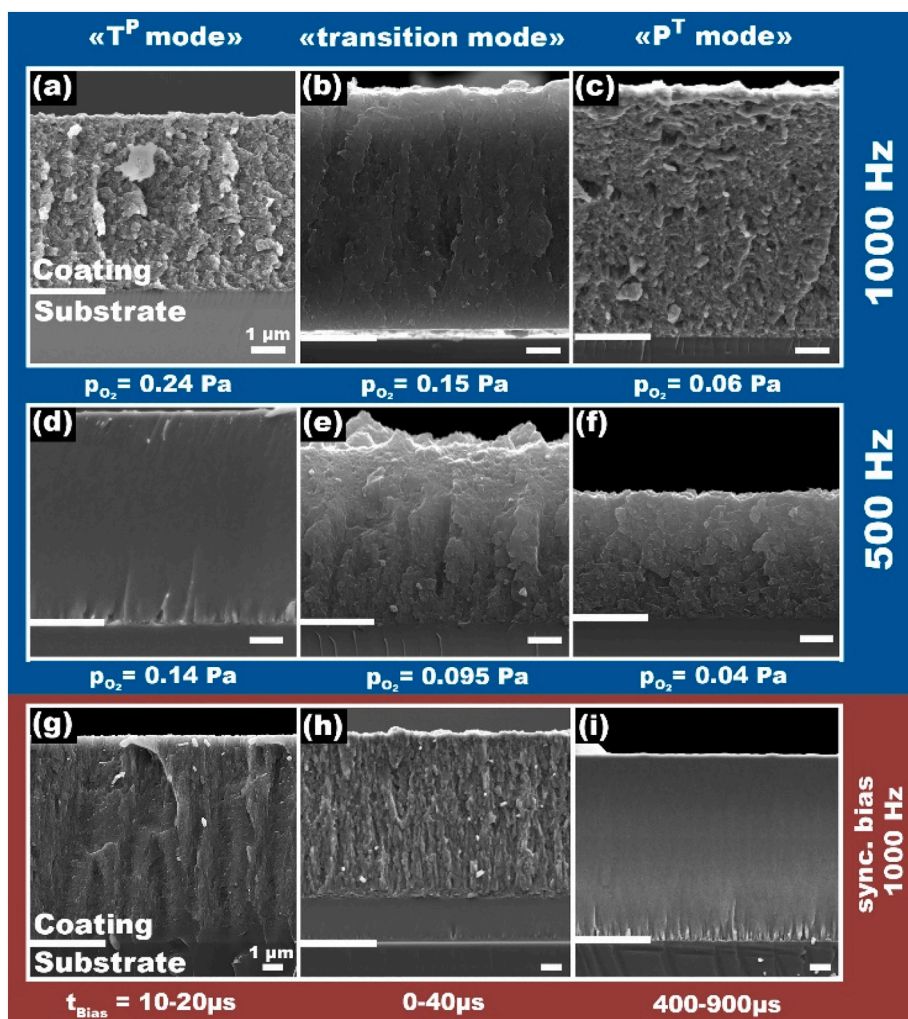


Fig. 7. Cross-sectional SEM images of coatings (on silicon substrates) prepared from an $\text{Al}_{0.98}\text{W}_{0.02}$ target in Ar/O_2 atmosphere operated at a frequency of (a-c) 1000 Hz and (d-f) 500 Hz in T^{T} , transition, and T^{P} mode, respectively. The individual oxygen partial pressure to each coating is given below the corresponding image. All coatings presented in (a-f) were prepared using a constant bias potential of -50 V. Fracture cross-sections of coatings prepared with $f = 1000$ Hz, $p_{\text{O}_2} = 0.15$ Pa and a bias potential synchronized to specific timeframes after the cathode pulse ignition are given in (g), (h), and (i), with the bias potential active between $t = 10\text{--}20$ μs , $t = 0\text{--}40$ μs , and $t = 400\text{--}900$ μs of the 1000 μs long pulse duration, respectively.

Three additional coatings were prepared with $f = 1000$ Hz ($t_{\text{on}} = 75$ μs , duty cycle = 7.5%) at oxygen partial pressures of 0.24, 0.15 and 0.06 Pa, where the $\text{Al}_{0.98}\text{W}_{0.02}$ target again was operated in the T^{P} , T, and P^{T} mode, respectively, corresponding to the hysteresis curve shown in Fig. 6a. Both hysteresis curves show in principle an identical poisoning behavior as observed for those recorded in the system used for plasma diagnostics (Fig. 2). The higher oxygen flow is mainly necessary to accommodate for the larger cathode size (6 in.) and system volume. Nevertheless, the narrowing trend of the hysteresis curves with reduced duty cycles is comparable with the curves shown in Fig. 2. However, the previously observed increase in the target voltage for lower values of the duty cycle at a constant power of $1 \text{ kW}/\text{cm}^2$ was not measured. These six coatings were prepared using $U_{\text{bias}} = -50$ V DC. In addition, coatings were prepared with $f = 1000$ Hz ($t_{\text{on}} = 75$ μs , duty cycle = 7.5%) and $p_{\text{O}_2} = 0.15$ Pa (transition mode) by synchronizing the bias potential to three different timeframes with respect to the cathode signal. Therefore, the on-time of the bias pulse was synchronized to 10–20 μs , 0–40 μs , and 400–900 μs after the cathode pulse ignition.

A duty cycle of 7.5% ($f = 1000$ Hz) leads to coatings with a growth morphology suggesting for a significant fraction of a metallic phase, which agrees with the metallic cross-sectional appearance and further XRD studies conducted (not shown in this work). This type of coating is obtained irrespective of all three oxygen partial pressures used and thus also the target operation modes T^{P} , T, and P^{T} (see SEM fracture cross-sections of single side-coated Si substrates in Figs. 7a, b, and c, respectively). Fig. 7d, e, and f include the SEM fracture cross-sections of the

coatings prepared with $f = 500$ Hz. Especially the coating prepared with $p_{\text{O}_2} = 0.14$ Pa reveals a very dense and featureless growth morphology. Moreover, since here the target operates in the T^{P} mode, this is also the thickest coating of this series. The growth morphology of the other two coatings ($p_{\text{O}_2} = 0.095$ and 0.04 Pa) again suggests for the presence of a metallic phase – as could be proven by XRD (not shown in this work) – despite operating the target in the transition (see Fig. 7e) or even the P^{T} (see Fig. 7f) mode. This is because the provided oxygen partial pressure is too low for a stoichiometric oxide to form on the substrate surface, yet sufficient to alter the target surface chemistry.

To further study the effect of a synchronized bias potential on the phase formation and thin film growth, we selected the most promising sputtering conditions in terms of process stability and oxygen partial pressure obtained for a continuous bias signal as a reference. Therefore, we chose a frequency of 1000 Hz and an on-time of 75 μs . This leads to a coating with the smallest fraction of metallic phase, a fine-grained growth morphology, and a slightly transparent, grayish appearance using dc-bias (see Fig. 7b). Thus, synchronizing the bias potential to the promising time segments, mentioned in Fig. 5 should increase the alumina phase formation and the overall oxygen content within the coating.

Using the synchronized bias concept drastically increases the quality of the coatings, represented by their growth morphologies in Fig. 7g, h, and i. An on-time of the bias pulse between 10 and 20 μs after the HiPIMS pulse ignition leads to a more dense and columnar growth morphology (see Fig. 7g). This beneficial aspect on oxide film growth upon synchronizing the bias to the timeframe could be explained by the

fact that there should be an overall increased arrival of oxygen ions over Al ions due to the slight dip of the Al ion counts at $t \sim 0 \mu\text{s}$ (see Fig. 5b). Furthermore, an on-time of the bias pulse synchronized from 0 to $40 \mu\text{s}$ of the cathode pulse initially leads to a completely featureless growth morphology up to a coating thickness of $\sim 2 \mu\text{m}$, after which the morphology changes and again suggests for a larger fraction of a metallic phase (see Fig. 7h). The abrupt change in the growth morphology can be directly related to an erosion of the oxide layer on the target surface, which is related to a change of the poisoning state - the transition zone to metallic mode. Therefore, the coating morphology in Fig. 7h is direct connected to the poisoning state and not induced by the influence of the synchronized bias pulse. Using a bias pulse synchronized from 400 to $900 \mu\text{s}$ after the pulse ignition, leads to a completely featureless growth morphology (see Fig. 5i). Within this last timeframe, Al^+ , $^{32}\text{O}_2^+$, and Ar^+ ions compose the majority of the ion flux arriving at the substrate surface. The amorphous morphology of the coating is basically linked to the pronounced Al^+ and $^{32}\text{O}_2^+$ ion supply and not by the high Ar^+ fraction. This stays in agreement with Fig. 7e and 7f even though, the influence of Ar^+ ions on the microstructure is significantly higher due to the long off-set ($1925 \mu\text{s}$) of the 500 Hz deposition, the coatings are still crystalline and just the high oxygen partial pressure (see Fig. 7d) lead to a featureless growth. Moreover, the deposition process was found to be extremely stable throughout the deposition of a $7 \mu\text{m}$ thick coating for these deposition conditions. Synchronized bias offers its ability to enhance the chemical composition and the morphology of the coating especially in lab scale chambers, whereas the distance from cathode to substrate holder is more or less constant. In industrial sized chambers synchronized bias is more challenging due to the planetary-type of the substrate rotation which causes in a variation of the substrate to cathode distance and leads in a inhomogeneous ion bombardment [39,40].

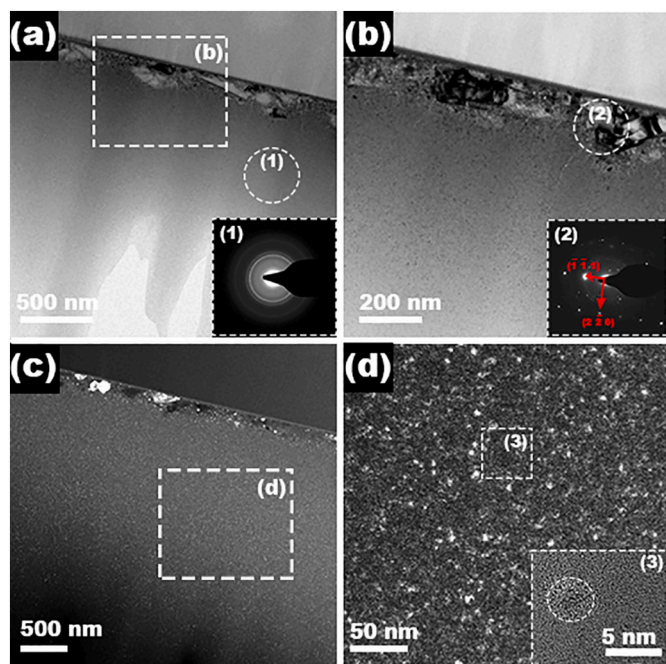


Fig. 8. (a) Cross-sectional TEM bright field image of the $(\text{Al}_{0.98}\text{W}_{0.02})_2\text{O}_3$ -based coating on silicon substrate deposited at $f = 500 \text{ Hz}$, $t_{\text{on}} = 75 \mu\text{s}$ and an oxygen partial pressure of $p_{\text{O}_2} = 0.14 \text{ Pa}$. (b) represents a closer view of the interface near region shown in (a). SAED patterns (1) and (2) of the marked sample regions show an almost amorphous coating on a crystalline, Al enriched interface region. (c) Shows a cross-sectional dark field TEM image of the sample region shown in (a) and (b). (d) Shows a higher magnification of the amorphous-like coating in inset (d) and marks the region used for a further (3) HR-TEM inset, showing an Al_2O_3 grain surrounded by an amorphous matrix.

To investigate the metallic phase content in the coatings, previously observed in SEM fracture-cross sections as well as in complementary XRD studies, in more detail, TEM microanalysis was performed on the coating prepared with $f = 500 \text{ Hz}$ ($t_{\text{on}} = 75 \mu\text{s}$, duty cycle = 3.75%) and an oxygen partial pressure of $p_{\text{O}_2} = 0.14 \text{ Pa}$ (see corresponding fracture cross-section in Fig. 7d).

The cross-sectional bright-field TEM image presented in Fig. 8a shows the almost amorphous growth of the coating [41], additionally underlined by the SAED inset (1), as well as the predominantly crystalline region close to the interface to the Si substrate. The latter is presented in Fig. 8b at higher magnification, with the corresponding SAED (see inset (2)) now covering the entire interface region, showing a clearly crystalline Al structure (Fm3m, ZA [1, 1, 2], FN [1, 1, 2]), indicated by distinct diffraction spots. Furthermore, smaller crystalline parts surrounded by an amorphous matrix can also be recognized further away from this interface within the “bulk” part of the coating, especially visible in the dark-field TEM micrograph presented in Fig. 8c. At even higher magnification of the dark-field TEM image around inset (d) shown in Fig. 8d, the nano-crystalline structure becomes even more clear through the speckled appearance, indicating the nano-sized electron-diffracting (i.e. crystalline) regions. The additional HR-TEM acquisition of the small region marked with (3) further underlines the presence of these small crystallites, see inset (3) in Fig. 8d. Complementary Fast Fourier Transformation of the high-resolution image (not shown) suggests that the small, $\sim 5 \text{ nm}$ wide nanocrystals are comprised of the $\gamma\text{-Al}_2\text{O}_3$ phase. Detailed chemical investigations by STEM-EDS mapping (Fig. 9a to c) show a higher Al and W content located in the interface-near region to the substrate followed by a rather uniform elemental distribution. This suggests that the crystallites at the interface are basically Al enriched regions surrounded by Al_2O_3 , which is in good agreement with previous studies by Barna et al. [42]. Crystalline Al has essentially no solubility for O, hence only Al_2O_3 based phases can be formed [43]. The SEM-EDS line scan across the entire coating thickness, Fig. 9d, clearly shows the Al-rich interface-near region and the chemically homogeneous subsequent part of the coating.

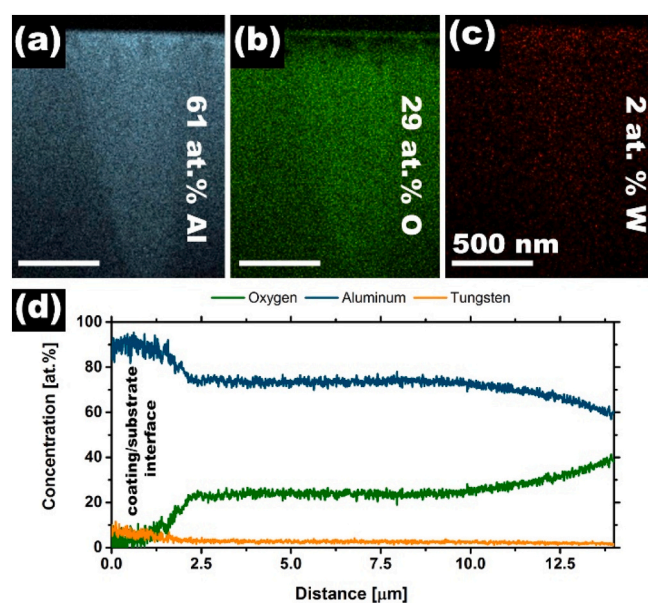


Fig. 9. STEM-EDS mapping for (a) aluminum, (b) oxygen, and (c) tungsten of the cross section on the coating prepared from an $\text{Al}_{0.98}\text{W}_{0.02}$ target with $f = 500 \text{ Hz}$ and $p_{\text{O}_2} = 0.14 \text{ Pa}$. The corresponding SEM fracture cross-section is given in Fig. 7d. (d) SEM-EDS - line scan of the sample shown in (a-c) over the entire cross-sectional area. The Al rich region near the silicon substrate interface is clearly detectable.

4. Conclusion

The process stability and oxygen content taking part at the deposition process can be increased by alloying a specific amount of tungsten (2 at.%) inside the target. Dependent on the mode of operation and the target power density (HiPIMS or DCMS) the oxygen partial pressure can be increased to more than 200% compared with a pure aluminum target (purity 99.8%). Varying the frequency leads to a decrease of the hysteresis width and to an increase of average voltage. Furthermore, a shift of the hysteresis curve of the tungsten containing coatings to higher oxygen partial pressures can be detected, compared to pure aluminum targets. This can be explained once by higher peak power density, using lower frequencies. A further reason is the sputter yield amplification utilized by doping the targets with tungsten. A third cause is the return of the metal ions on the target surface, which leads to an abrasion of the insulating ceramic layer on the target surface. Thus, tungsten retards target poisoning and allows the usage of higher oxygen partial pressures. The enlarging of the transition zone influences positive especially DCMS coatings due to the increased oxygen partial pressure while a constant target abrasion takes place. HiPIMS coatings reacts more sensitive on the change of the target state. This points out in the metallic coating growth in the interface near region followed by amorphous/ceramic deposition conditions. A hysteresis free deposition process couldn't be achieved in this study. Detailed plasma analyses of the metallic, transition and poisoned mode for different duty cycles using ion mass spectroscopy shows the lowest amount of O^+ and O_2^+ in the metallic near region (highest oxygen partial pressure). It turns out that the oxygen of the target surface oxide in poisoned mode as well as in the transition mode is easier to ionize compared to oxygen gas. Especially in poisoned mode the ionization of O^{16+} increases significantly. Biasing the substrate holder allows the attraction of a similar amount of oxygen and aluminum ions and can force a stoichiometric Al_2O_3 ratio. More detailed information of the ionization states was gained by time of flight ion mass spectroscopy. Based on this measurement three promising time ranges with a higher amount of ionized oxygen compared to aluminum ions are available. Particularly the afterglow ("off-time") between 400 and 900 μs offers a promising amount of $^{32}O_2^+$ and $^{27}Al^+$. The presence of low amount of aluminum neutrals doesn't influence the amorphous ($Al_{0.98}W_{0.02}O_{3\pm\delta}$) coating growth. SEM investigations shows that the ionization rate of reactive gases, using $f = 1000$ Hz, is too low for a stoichiometric Al_2O_3 , the presence of metallic species dominates. Decreasing the frequency to 500 Hz leads to an almost amorphous ($Al_{0.98}W_{0.02}O_{3\pm\delta}$) deposition in the "transition to poisoned mode", formed from the highest oxygen partial pressure and not from the oxygen provided by the target surface oxide. Detailed TEM-investigations exposes a metallic growth at the interface and a morphologically change of the coating properties from metallic to amorphous oxide deposition. HR-TEM points out that small (averaged grain size of 5 nm) $\gamma-Al_2O_3$ grains are embedded in the amorphous matrix. STEM and SEM EDS investigations reveals an under stoichiometric aluminum to oxygen ratio. Overall tungsten alloyed aluminum targets retard poisoning effects this benefits especially DCMS processes due to the constant target abrasion and is more complex for HiPIMS (abrupt changes in the coating morphology). To increase oxygen content the usage of synchronized bias in HiPIMS processes combined with micro alloyed targets can be one of the key technologies and may offer the change from amorphous to fully crystalline $\gamma(\alpha?)Al_2O_3$ coatings.

CRedit authorship contribution statement

S. Kagerer: Conceptualization, Writing – original draft, Data curation, Investigation, Visualization. **L. Zauner:** Investigation, Writing – review & editing. **T. Wojcik:** Investigation. **S. Kolozsvári:** Resources. **T. Kozák:** Investigation, Writing – review & editing. **J. Čapek:**

Investigation, Writing – review & editing. **P. Zeman:** Investigation, Writing – review & editing. **H. Riedl:** Writing – review & editing, Visualization, Supervision, Project administration. **P.H. Mayrhofer:** Writing – review & editing, Supervision, Project administration, Funding acquisition.

Declaration of competing interest

The authors declare that they have no known competing financial interests or personal relationships that could have appeared to influence the work reported in this paper.

Acknowledgments

We acknowledge the support by the X-ray Center (XRC) of the TU Wien, the support by the University Service Center for Transmission Electron Microscopy (USTEM), TU Wien, as well as by Plansee Composite Materials GmbH. The financial support by the Austrian Federal Ministry for Digital and Economic Affairs and the National Foundation for Research, Technology, and Development is gratefully acknowledged (Christian Doppler Laboratory "Surface Engineering of high-performance Components"). The plasma diagnostics experiments done at University of West Bohemia were supported by the European Structural and Investment Funds under project no. CZ.02.1.01/0.0/0.0/17.048/0007267. The authors acknowledge TU Wien Bibliothek for financial support through its Open Access Funding Programme."

Appendix A. Supplementary data

Supplementary data to this article can be found online at <https://doi.org/10.1016/j.surfcoat.2021.127467>.

References

- [1] R.F. Bunshah, R.J. Schramm, Alumina deposition by activated reactive evaporation, *Thin Solid Films* 40 (1977) 211–216, [https://doi.org/10.1016/0040-6090\(77\)90120-1](https://doi.org/10.1016/0040-6090(77)90120-1).
- [2] P. Eklund, M. Sridharan, G. Singh, J. Böttiger, Thermal stability and phase transformations of γ -amorphous-Al₂O₃ thin films, *Plasma Process. Polym.* 6 (2009) 907–911, <https://doi.org/10.1002/ppap.200932301>.
- [3] J.M. Andersson, E. Wallin, U. Helmersson, U. Kreissig, E.P. Mürger, Phase control of Al₂O₃ thin films grown at low temperatures, *Thin Solid Films* 513 (2006) 57–59, <https://doi.org/10.1016/j.tsf.2006.01.016>.
- [4] C.M. Koller, M. Stueber, P.-H. Mayrhofer, Progress in the synthesis of Al- and Cr-based sesquioxide coatings for protective applications, *J. Vac. Sci. Technol. A* 37 (2019), 060802, <https://doi.org/10.1116/1.5120793>.
- [5] M. Åstrand, T.I. Selinder, F. Fietzke, H. Klostermann, PVD-Al₂O₃-coated cemented carbide cutting tools, *Surf. Coat. Technol.* 188–189 (2004) 186–192, <https://doi.org/10.1016/j.surfcoat.2004.08.021>.
- [6] I. Levin, D. Brandon, Metastable alumina polymorphs: crystal structures and transition sequences, *J. Am. Ceram. Soc.* 81 (2005) 1995–2012, <https://doi.org/10.1111/j.1151-2916.1998.tb02581.x>.
- [7] J.M. McHale, A. Auroux, A.J. Perrotta, A. Navrotsky, Surface energies and thermodynamic phase stability in nanocrystalline aluminas, *Science* 277 (80) (1997) 788–789, <https://doi.org/10.1126/science.277.5327.788>.
- [8] J.A. García-Valenzuela, R. Rivera, A.B. Morales-Vilches, L.G. Gerling, A. Caballero, J.M. Asensi, C. Voz, J. Bertomeu, J. Andreu, Main properties of Al₂O₃ thin films deposited by magnetron sputtering of an Al₂O₃ ceramic target at different radio-frequency power and argon pressure and their passivation effect on p-type c-Si wafers, *Thin Solid Films* 619 (2016) 288–296, <https://doi.org/10.1016/j.tsf.2016.10.049>.
- [9] G. Hoetzsch, F. Fietzke, K. Goedicke, Effect of the substrate temperature on the structure and properties of Al₂O₃ layers reactively deposited by pulsed magnetron sputtering, *Surf. Coat. Technol.* 82 (1996) 169–175, [https://doi.org/10.1016/0257-8972\(95\)00270-7](https://doi.org/10.1016/0257-8972(95)00270-7).
- [10] T. Kohara, H. Tamagaki, Y. Ikari, H. Fujii, Deposition of α -Al₂O₃ hard coatings by reactive magnetron sputtering, *Surf. Coat. Technol.* 185 (2004) 166–171, <https://doi.org/10.1016/j.surfcoat.2003.11.017>.
- [11] J.M. Schneider, W.D. Sproul, Crystalline alumina deposited at low temperatures by ionized magnetron sputtering, *J. Vac. Sci. Technol. A Vacuums, Surfaces, Film.* A 15 (1997) 1084, <https://doi.org/10.1116/1.580434>.
- [12] C.M. Koller, R. Hahn, B. Widrig, J. Ramm, S. Kolozsvári, J. Paulitsch, P. H. Mayrhofer, Triggering the Phase Evolution Within (Al,Cr)2O3-based Coatings

- by Alloying and Microstructural Concepts Initiierung von Phasenstrukturen in Al-Cr-basierten Oxiden durch Mikrostruktur- und Legierungskonzepte, BHM Berg- und Hüttenmännische Monatshefte 161 (2016) 325–329, <https://doi.org/10.1007/s00501-016-0506-2>.
- [13] E. Wallin, T.I. Selinder, M. Elfving, U. Helmersson, Synthesis of α -Al₂O₃ thin films using reactive high-power impulse magnetron sputtering, *Epl.* 82 (2008), <https://doi.org/10.1209/0295-5075/82/36002>.
- [14] D. Güttler, B. Abendroth, R. Gröttschel, W. Möller, D. Depla, Mechanisms of target poisoning during magnetron sputtering as investigated by real-time in situ analysis and collisional computer simulation, *Appl. Phys. Lett.* 85 (2004) 6134–6136, <https://doi.org/10.1063/1.1835002>.
- [15] C.M. Koller, V. Dalbauer, A. Kirnbauer, M. Sauer, S. Kolozsvári, J. Ramm, P. H. Mayrhofer, Impact of Si and B on the phase stability of cathodic arc evaporated Al_{0.70}Cr_{0.30}-based oxides, *Scr. Mater.* 152 (2018) 107–111, <https://doi.org/10.1016/j.scriptamat.2018.04.018>.
- [16] E. Wallin, U. Helmersson, Hysteresis-free reactive high power impulse magnetron sputtering, *Thin Solid Films* 516 (2008) 6398–6401, <https://doi.org/10.1016/j.tsf.2007.08.123>.
- [17] J. Capek, S. Kadlec, Return of target material ions leads to a reduced hysteresis in reactive high power impulse magnetron sputtering: Experiment, *J. Appl. Phys.* 121 (2017), <https://doi.org/10.1063/1.4977816>.
- [18] W.D. Sproul, D.J. Christie, D.C. Carter, Control of reactive sputtering processes, *Thin Solid Films* 491 (2005) 1–17, <https://doi.org/10.1016/j.tsf.2005.05.022>.
- [19] D. Lundin, K. Sarakinos, An introduction to thin film processing using high-power impulse magnetron sputtering, 2012, <https://doi.org/10.1557/jmr.2012.8>.
- [20] C.M. Koller, V. Dalbauer, A. Schmelz, R. Raab, P. Polcik, J. Ramm, P.H. Mayrhofer, Structure, mechanical properties, and thermal stability of arc evaporated (Al_{1-x}Cr_x)₂O₃ coatings, *Surf. Coat. Technol.* 342 (2018) 37–47, <https://doi.org/10.1016/j.surfcoat.2018.02.077>.
- [21] S. Berg, A.M. Barklund, B. Gelin, C. Nender, I. Katardjiev, Atom assisted sputtering yield amplification, *J. Vac. Sci. Technol. A* 10 (1992) 1592–1596, <https://doi.org/10.1116/1.578049>.
- [22] M. Austgen, D. Koehl, P. Zalden, T. Kubart, T. Nyberg, A. Pflug, M. Siemers, S. Berg, M. Wuttig, Sputter yield amplification by tungsten doping of Al₂O₃ employing reactive serial co-sputtering: process characteristics and resulting film properties, *J. Phys. D: Appl. Phys.* 44 (2011), <https://doi.org/10.1088/0022-3727/44/34/345501>.
- [23] E. Wallin, J.M. Andersson, V. Chirita, U. Helmersson, Effects of additives in α - and θ -alumina: an ab initio study, *J. Phys. Condens. Matter.* 16 (2004) 8971–8980, <https://doi.org/10.1088/0953-8984/16/49/012>.
- [24] B. Kohlhauser, H. Riedl, C.M. Koller, V. Paneta, S. Kolozsvári, P.H. Mayrhofer, How microalloying of the Al target can improve process and film characteristics of sputtered alumina, *Surf. Coat. Technol.* 393 (2020), 125762, <https://doi.org/10.1016/j.surfcoat.2020.125762>.
- [25] L. Zauner, P. Ertelthaler, T. Wojcik, H. Bolvardi, S. Kolozsvári, P.H. Mayrhofer, H. Riedl, Reactive HIPIMS deposition of Ti-Al-N: influence of the deposition parameters on the cubic to hexagonal phase transition, *Surf. Coat. Technol.* (2019), 125007, <https://doi.org/10.1016/j.surfcoat.2019.125007>.
- [26] Hiden Analytical Ltd, EQP and EQS Analysers, 2020.
- [27] Hiden Analytical Ltd. 2019 personal communication, (n.d.).
- [28] A. Anders, Discharge physics of high power impulse magnetron sputtering, *Surf. Coat. Technol.* 205 (2011) S1–S9, <https://doi.org/10.1016/j.surfcoat.2011.03.081>.
- [29] A. Anders, Tutorial: reactive high power impulse magnetron sputtering (R-HiPIMS), *J. Appl. Phys.* 121 (2017), <https://doi.org/10.1063/1.4978350>.
- [30] J.T. Gudmundsson, N. Brenning, D. Lundin, U. Helmersson, High power impulse magnetron sputtering discharge, *J. Vac. Sci. Technol. A* 30 (2012), 030801, <https://doi.org/10.1116/1.3691832>.
- [31] J. Lin, J.J. Moore, W.D. Sproul, B. Mishra, Z. Wu, Modulated pulse power sputtered chromium coatings, *Thin Solid Films* 518 (2009) 1566–1570, <https://doi.org/10.1016/j.tsf.2009.09.118>.
- [32] B. Szapiro, J.J. Rocca, Electron emission from glow-discharge cathode materials due to neon and argon ion bombardment, *J. Appl. Phys.* 65 (1989) 3713–3716, <https://doi.org/10.1063/1.342600>.
- [33] D. Depla, X.Y. Li, S. Mahieu, R. De Gryse, Determination of the effective electron emission yields of compound materials, *J. Phys. D: Appl. Phys.* (2008), <https://doi.org/10.1088/0022-3727/41/20/202003>.
- [34] R. Ganesan, B. Treverrow, B. Murdoch, D. Xie, A.E. Ross, J.G. Partridge, I. S. Falconer, D.G. McCulloch, D.R. McKenzie, M.M.M. Bilek, Duty cycle control in reactive high-power impulse magnetron sputtering of hafnium and niobium, *J. Phys. D: Appl. Phys.* 49 (2016), <https://doi.org/10.1088/0022-3727/49/24/245201>.
- [35] T. Kubart, M. Aiempakanit, J. Andersson, T. Nyberg, S. Berg, U. Helmersson, Studies of hysteresis effect in reactive HiPIMS deposition of oxides, *Surf. Coat. Technol.* 205 (2011) S303–S306, <https://doi.org/10.1016/j.surfcoat.2011.01.019>.
- [36] S. Kadlec, J. Capek, Return of target material ions leads to a reduced hysteresis in reactive high power Return of target material ions leads to a reduced hysteresis in reactive high power impulse magnetron sputtering: model, *J. Appl. Phys.* 171910 (2017), <https://doi.org/10.1063/1.4977815>.
- [37] D.R. Lide, CRC Handbook of Chemistry and Physics, 84th edition, CRC Press. (2003). doi:<https://doi.org/10.1136/oem.53.7.504>.
- [38] N. Nedfors, O. Vozniy, J. Rosen, Effect of synchronized bias in the deposition of TiB₂ thin films using high power impulse magnetron sputtering, *J. Vac. Sci. Technol. A* 36 (2018), 031510, <https://doi.org/10.1116/1.5003194>.
- [39] M. Panjan, T. Peterman, M. Čekada, P. Panjan, Simulation of a multilayer structure in coatings prepared by magnetron sputtering, *Surf. Coat. Technol.* 204 (2009) 850–853, <https://doi.org/10.1016/j.surfcoat.2009.08.026>.
- [40] M. Panjan, Influence of substrate rotation and target arrangement on the periodicity and uniformity of layered coatings, *Surf. Coat. Technol.* 235 (2013) 32–44, <https://doi.org/10.1016/j.surfcoat.2013.06.126>.
- [41] M.G.J. Müller, F. Nahif, J. Mayer, J.M. Schneider, Transmission electron microscopy investigation of the effect of Si alloying on the thermal stability of amorphous alumina thin films deposited by filtered cathodic arc deposition, *Surf. Coat. Technol.* 257 (2014) 338–347, <https://doi.org/10.1016/j.surfcoat.2014.07.088>.
- [42] P.B. Barna, M. Adamik, Fundamental structure forming phenomena of polycrystalline films and the structure zone models, *Thin Solid Films* 317 (1998) 27–33, [https://doi.org/10.1016/S0040-6090\(97\)00503-8](https://doi.org/10.1016/S0040-6090(97)00503-8).
- [43] H.A. Wriedt, The Al-O (aluminum-oxygen) system, *Bulletin of Alloy Phase Diagrams* 6 (1985) 548–553, <https://doi.org/10.1007/BF02887157>.